Received: 9 November 2023 | Revised: 22 December 2023 | Accepted: 26 January 2024

DOI: 10.1002/pc.28205

RESEARCH ARTICLE

spe INSPIRING PLASTICS PROFESSIONALS Polymer COMPOSITES WILEY

Modifying the properties of polyamide 6 with high-performance environmentally friendly nano- and microsized reinforcing materials

László Mészáros[1,2] | Ádám Bezerédi[1] | Roland Petrény[1]

[1]Department of Polymer Engineering, Faculty of Mechanical Engineering, Budapest University of Technology and Economics, Budapest, Hungary

[2]HUN-REN-BME Research Group for Composite Science and Technology, Budapest, Hungary

Correspondence
László Mészáros, Department of Polymer Engineering, Faculty of Mechanical Engineering, Budapest University of Technology and Economics, Műegyetem rkp. 3., H-1111 Budapest, Hungary.
Email: meszaros@pt.bme.hu

Funding information
Nemzeti Kutatási, Fejlesztési és Innovációs Alap; Magyar Tudományos Akadémia; Nemzeti Kutatási Fejlesztési és Innovációs Hivatal; Ministry of Culture and Innovation of Hungary from the National Research, Development, and Innovation Fund, Grant/Award Number: TKP-6-6/PALY-2021; New National Excellence Program of the Ministry for Culture and Innovation from the source of the National Research, Development, and Innovation Fund, Grant/Award Number: ÚNKP-23-5-BME-434; European Union's Horizon 2020 research and innovation program under Marie Skłodowska-Curie grant, Grant/Award Number: 872152 (GREEN MAP)

Abstract

In this study, we investigated the morphological and mechanical properties of hybrid composites with a polyamide 6 (PA6) matrix and reinforced with basalt fibers (BFs) and halloysite nanotubes (HNTs). The presence of reinforcing materials fundamentally changed the behavior of the molecules, which was morphologically manifested in the change in the ratio of the rigid and the mobile amorphous phase. The x-ray diffraction and transmission electron microscopic images showed the crystal nucleating effect of the halloysite nanotubes. Based on these, we concluded that around the basalt fibers, an interphase is formed, while around the nanoparticles, a two-layer interphase is created, the inner layer of which is semicrystalline, while the outer layer is rigid amorphous (RA). The nanoparticles are surrounded by a semicrystalline interphase, which is surrounded by an RA interphase. This overlaps with the interphase of the basalt fibers, therefore the halloysite nanotubes can effectively help the stress transfer from the matrix to the basalt fibers. The mechanical properties of the samples also reflected this: the hybrid composites had a significantly higher tensile modulus, tensile strength, and an unchanged elongation at break compared to the composite reinforced with only basalt fiber.

Highlights

- Environmentally friendly polyamide 6 matrix hybrid composites were prepared.
- Uniform distribution of halloysite nanotubes was achieved.
- Enhanced mechanical properties were observed for hybrid composites.
- Halloysite nanotubes aid stress transfer from matrix to basalt fibers.
- Halloysite nanotubes act as crystalline nucleating agents.

KEYWORDS

basalt fiber, halloysite, hybrid composite, interphase, mechanical properties

1 | INTRODUCTION

During the third industrial revolution in the 20th century, the environmental awareness of industry and the importance of environmental protection became an issue. With these principles in mind, the plastics industry strives to reduce its ecological footprint by reducing the environmental impact of production, recycling post-production waste, and choosing the materials of finished products. The latter, particularly in the automotive industry, has implications for reducing emissions during end-use—indirectly through weight reduction—and reducing the technological steps and resource requirements of producing finished products and their raw materials.[1–3]

Polymer composites have excellent mechanical properties compared to their weight. Glass and carbon fibers are the most common fibrous reinforcement materials for composites. Although the latter is a reinforcing material with excellent mechanical and thermal properties, its production is highly energy-intensive, polluting (high CO_2 emissions), and it is challenging to recycle. Therefore, it is worth exploring basalt fiber (BF) as a fiber reinforcement material for composites and its applicability in composites, as it can offer an excellent alternative to carbon fiber in specific applications.[4–7] The raw material for basalt fiber is natural volcanic basalt rock, which is easily and economically accessible by surface mining and is abundantly available. The fibers are produced directly from the molten rock without additives and do not require several technological steps. In combination with a biodegradable matrix material, BF increases the mineral content of compost during composting and has potential medical applications due to its biocompatibility. BF is comparable to glass fiber in terms of its mechanical properties.[8,9]

To further strengthen composites, nanomaterials can be used in addition to the widely used microfiber reinforcement. For example, hybrid composite products made this way are already commercially available in the sports industry. The presence of nanoparticles increases performance and allows the production of high-strength products with lower mass. Nanomaterials can help transfer the load between the fibers and the matrix[10–12] when used in fiber-reinforced hybrid composites.

Currently, carbon nanotubes (CNTs) are the most widely used. Still, halloysite nanotubes (HNTs) can be an excellent environmentally friendly alternative to CNTs, which are much more expensive and more complicated to recycle.[10] HNTs consist of coiled disks with different polarity inside and outside, with alumnol on the inner surface and a silane compound on the outer surface to aid the adhesion of the matrix material to the HNT.[11] The dimensions of these hollow nanotubes can vary widely, with an inner diameter of 1–30 nm, an outer diameter of 30–50 nm, and a length of 100–2000 nm. Using HNTs in composites may have several advantages besides their strength-enhancing effect. Previous research has shown that its use is also suitable for medical applications; HNTs are not harmful to health, making them an excellent structural material for tissue engineering and pharmaceutical applications.[12] However, HNTs have a high specific volume in addition to their small size, and due to these properties, they tend to form aggregates, which may reduce the surface area available for adhesion to the matrix material. However, using them in hybrid composites has the advantage that the microfibers, besides their reinforcing effect, greatly facilitate the dispersion of nano-sized reinforcing materials. The application of microfibers increases the shear forces during the compounding of the final product, thus increasing the dispersion of the nanofibers in the matrix material.[13–15]

However, these hybrid composites mostly have a thermoset polymer matrix, making their processing difficult and costly. Therefore, using a thermoplastic matrix material such as polyamide 6 (PA6) is preferable. Due to its excellent mechanical, thermal, and chemical resistance properties, PA6 is widely used in the automotive industry, both as a material for gears and bearings and as a material for components of the engine compartment. The use of PA6 as a matrix material offers several additional advantages over thermosetting polymers from a manufacturing technology point of view. The most common processing methods to produce composite products with a thermoplastic matrix are extrusion and injection molding. The latter has the advantage that it can be used to produce parts with more complex geometries in large quantities and reproducible quality in an automatic cycle, with hardly any waste. Therefore, the manufacturability of hybrid nanocomposites with this technology is an important goal. Former research has shown that composites with a PA6 matrix and reinforced with basalt fiber and halloysite nanotubes are easily processable by injection molding, and the dispersion of the nanoparticles was much more uniform, which resulted in synergistic strengthening effects in the case of tensile and flexural loads.[16–19]

However, the structural causes for these mechanical properties in such multi-scale composites have been little researched to date. If there is a high-modulus material between the molecular chains, the movement of the molecular segments is inhibited due to the interfacial interaction. A rigid amorphous fraction (RAF) is created when the molecular segments are attached to the reinforcing materials or crystalline parts in the amorphous parts of the matrix. In the RAF phase, the mobility of polymer molecules is reduced. In other cases, if the reinforcing materials behave as crystal nucleating agents, crystalline regions surround them, and the crystalline regions are surrounded by RAF and these are embedded in the mobile amorphous molecular fraction (MAF). If crystallinity is high, RAF and MAF can also be found inside the spherulites or lamellae.

These show that a complex microstructure develops in these composites, which can affect the mechanical properties of the material in several ways.[20–22]

In the present study, we aim to thoroughly explore the microstructure of environmentally friendly micro- and nanoparticles and, based on this, to explain the effects of these reinforcing materials on the tensile properties of the nano- and hybrid composites.

2 | MATERIALS AND METHODS

The matrix material of the composite was Schulamid 6 MV 13F polyamide (PA6) produced by Schulman AG. The fiber reinforcement material was BCS 13.6.KV02 basalt fiber, which is produced by Kamenny Vek Ltd. Continuous fibers were manufactured and then they were cut to the appropriate length (nominal diameter: 13 μm, average length: 6 mm). The basalt fibers were treated with a silane surface treatment agent, which is usually applied for reinforcement materials used in epoxy. Based on the literature data, it can create a good adhesive bond with the PA6.[12]

For nanosized reinforcement, we used halloysite nanotubes ($H_4Al_2O_9Si_2{\cdot}2H_2O$), which were produced by Sigma-Aldrich Co. We used a marking scheme to make traceability and evaluation easier (Table 1):

The PA6 was dried for 4 h at 80°C in a Venticell LSIS-B2V/VC55 (MMM Group, USA) drying oven before use, according to the datasheet of the material. Extrusion was carried out with a Labtech LTE 26-44 (Labtech Engineering Co., Ltd., Thailand) twin-screw extruder. Rotation speed was 25 rpm for each material. The diameter of the screws was 26 mm, and their length/diameter ratio was 44. The temperature of the die was 240°C.

We injection molded EN ISO 527-2 1A type tensile specimens with a cross-section of 4 mm × 10 mm with an Arburg Allrounder 370 S 700-290 (Arburg GmbH, Germany) injection molding machine. The injection molding parameters were the same for all materials. The melt temperature was 270°C, the injection pressure was 1000 bar, and the holding pressure was 500 bar.

TABLE 1 Composition of the polyamide 6 matrix materials produced.

Sample	Basalt fiber content	Halloysite content
PA_ref	0 wt%	0 wt%
PA_H1	0 wt%	1 wt%
PA_H2	0 wt%	2 wt%
PA_H3	0 wt%	3 wt%
PABF_ref	30 wt%	0 wt%
PABF_H1	30 wt%	1 wt%
PABF_H2	30 wt%	2 wt%
PABF_H3	30 wt%	3 wt%

The melt flow index (MFI) tests were performed with a CEAST Modular Melt Flow 7027.000 (Instron, USA) capillary plastometer, according to the EN ISO 1133 standard. The length of the capillary was $l = 8$ mm, the radius of the capillary was $r = 10{,}475$ mm, the diameter of the piston was $D = 9$ mm, and the mass of the load was $m = 2{,}16$ kg. The test temperature was always 230°C. We performed five tests for each material.

Differential scanning calorimetry (DSC) was performed with a TA Instruments Q2000 (TA Instruments, USA) device. The samples were tested in the temperature range between 0°C and 250°C, with a heating rate of 5°C/min, in an inert gas atmosphere. The volumetric flow rate of the N_2 gas was set to 50 mL/min. TA Universal Analysis software was used to evaluate the data provided by the DSC device. The following equations were used to determine the phase ratio of the materials. The crystalline phase ratio (in the matrix) is:

$$X_c = \frac{\Delta H_m}{\Delta H_0\left(1-\phi_{f,wt}\right)} \times 100\,(\%), \tag{1}$$

where $\phi_{f,wt}$ is fiber content (wt%), X_c is the crystalline phase ratio, ΔH_m is the measured crystal melting enthalpy change, ΔH_0 is the crystal melting enthalpy change at a 100% crystalline phase ratio, which is 240 J/g for PA6.[13] The ratio of the MAF (in the matrix):

$$\mathrm{MAF} = \frac{\Delta c_p}{\Delta c_{p0}} \cdot \left(1-\phi_{f,wt}-X_c\right) \times 100\,(\%), \tag{2}$$

where Δc_p is the increment of the measured glass transition specific heat of the sample (J/g°C), Δc_{p0} is the increment of the measured glass transition specific heat of a fully amorphous material (J/g°C), which is 0.475 (J/g°C) for PA6.[11] The mass ratio of the RAF phase (in the matrix):

$$\mathrm{RAF} = 1 - \mathrm{MAF}\,(\%) - X_c \tag{3}$$

The lamellar thicknesses were calculated with the Gibbs–Thomson equation:

$$l = \frac{2\sigma_e}{\Delta H_m\,\rho_c\left(1-\frac{T_m}{T_{m,\infty}}\right)}, \tag{4}$$

where l is lamellar thickness, $\sigma_e = 5.7 \times 10^4\ \mathrm{J/m^2}$ is the surface free energy of the crystallite, $\Delta H_m = 241\ \mathrm{J/g}$ is

the enthalpy of crystal melting, $\rho_c = 1.230\,g/m^3$ is the density of the crystallite, $T_{m,\infty} = 533\,K$ is the theoretical melting point of an infinitely large crystallite and T_m is the melting peak from the measured DSC curve.[23–25]

The properties of PA6 used as a matrix are highly dependent on moisture content and the temperature of the material. Therefore, before testing, the specimens were conditioned in a desiccator for at least 4 weeks at 25°C and 50% relative humidity.[26]

For the x-ray diffraction analysis, a PANalytical X'pert Pro MPD x-ray diffractometer was used with a Cu K_α radiation source and an X'Celerator detector. The diffraction peaks at 9.4° and 29° belong to talc, an additive also present in the pure matrix and was not considered for further investigation. The amorphous baseline of the diffractograms was determined with the asymmetric least squares method. To distinguish the diffraction peaks, we used the pseudo-Voigt model. Then, we calculated the ratio of the α_1 and α_2 crystal planes, and the average crystallite size (L_{hkl}) perpendicular to the related planes with the Scherrer equation [14, 15]:

$$L_{hkl} = \frac{K \cdot \lambda}{\beta \cdot \cos\theta}, \tag{4}$$

where $K = 0.89$ (−) was the Scherrer constant, $\lambda = 0.154$ (nm) was the wavelength of the x-ray, and β is the full width at half maximum of the peak.

The tensile tests were performed on a Zwick-Z005 (Zwick GmbH & Co. KG, Germany) tensile tester, according to the EN ISO 527-1:2012 standard. Grip distance was 110 mm, while the test speed was 5 mm/min. The tests were performed on five specimens per sample at room temperature, and then the average and standard deviation were calculated based on the results of the individual measurements.

The fracture surface obtained after the tensile test was examined with a Jeol JSM-6380-LA (SEM, Jeol Ltd., Japan) scanning electron microscope with accelerating voltages of 10 and 15 kV at magnifications of 1000 and 10,000. The fracture surface of the specimens was coated with a thin layer of gold for electron microscopy.

3 | RESULTS AND DISCUSSION

3.1 | Melt properties

Generally, for a polymer, the MFI increases as the number of molecular interactions within the melt decreases, and decreases as the number of interactions increases. For filled and reinforced polymers, the MFI values are influenced by the strength of the filler-polymer interaction. Of course, in the case of nanoparticles, this depends on the connected surface, that is, whether the nanoparticles are present in an aggregate form or a dispersed state. In this case, whether the aggregates are impregnated with the matrix is of little importance because the nanoparticles in these aggregates do not move relative to each other, so neither can the polymer molecules, that is, these molecules do not participate in the flow itself—they are considered islands. Based on all of this, if there is a change in the distribution of the nanoparticles, it should also appear in the MFI.

The MFI of the materials containing only nanoparticles is hardly different compared to the matrix material. A slight, barely detectable decrease is ordinary, but no significant changes occurred (Table 2).

The basalt fiber reduced the MFI by approximately half, which indicates a good connection with the matrix material. In the case of hybrid composites, an apparent decrease can be observed with increasing nanotube content. Based on the above, this means that the degree of dispersion in hybrid composites is better than in the case of nanocomposites. The MFI results support the theory that the presence of the basalt fiber helped the distribution of the nanoparticles during processing.

3.2 | Differential scanning calorimetry

In the matrix of the nanocomposites, the ratio of the RAF, MAF, and crystalline fractions does not follow a clear trend, which can be explained by the random size and distribution of the halloysite nanotubes (Figure 1). In the matrix of the composite reinforced with basalt fiber only, the ratio of the RAF is significantly higher than in the pure PA6. This is because near the basalt fibers, the PA6 molecular segments are less mobile and therefore create an RAF interphase around the microfibers. When halloysite nanotubes are added to the basalt fiber–reinforced composite, the ratio of the different fractions

TABLE 2 The melt flow index of the nano- and hybrid composites with a PA 6 matrix.

Sample	MFI (g/10 min)
PA_ref	22.2 ± 0.2
PA_H1	21.7 ± 0.2
PA_H2	21.6 ± 0.4
PA_H3	21.5 ± 0.5
PABF_ref	10.8 ± 0.1
PABF_H1	10.1 ± 0.1
PABF_H2	9.8 ± 0.3
PABF_H3	8.7 ± 0.3

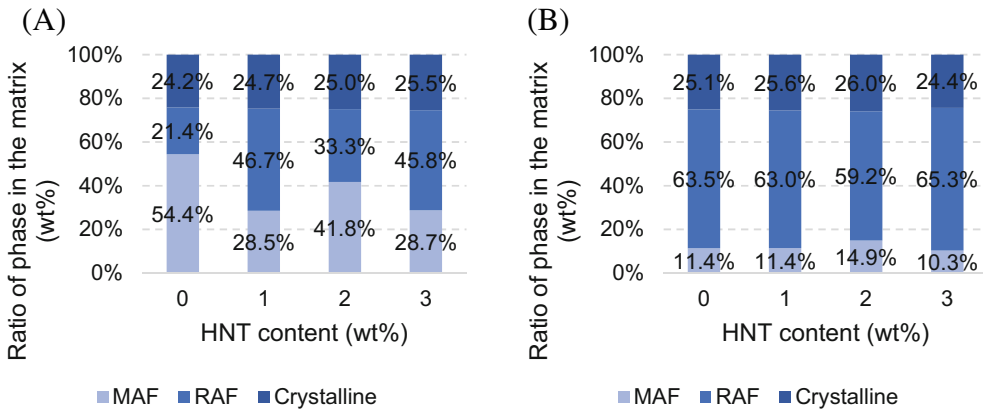

FIGURE 1 Mobile amorphous, rigid amorphous, and crystalline fractions (A) in the pure PA6 and the matrix of the nanocomposites, (B) in the matrix of the nanocomposites reinforced with only basalt fibers and in the hybrid nanocomposites.

TABLE 3 The thickness of the lamellae in the nano- and hybrid composites.

Sample	Peak temperature (°C)	Lamellar thickness (nm)
PA_ref	220.7	5.2
PA_H1	221.2	5.3
PA_H2	221.6	5.4
PA_H3	220.7	5.2
PA_BF	221.6	5.4
PA_BF_H1	222.2	5.5
PA_BF_H2	220.9	5.3
PA_BF_H3	221.8	5.4

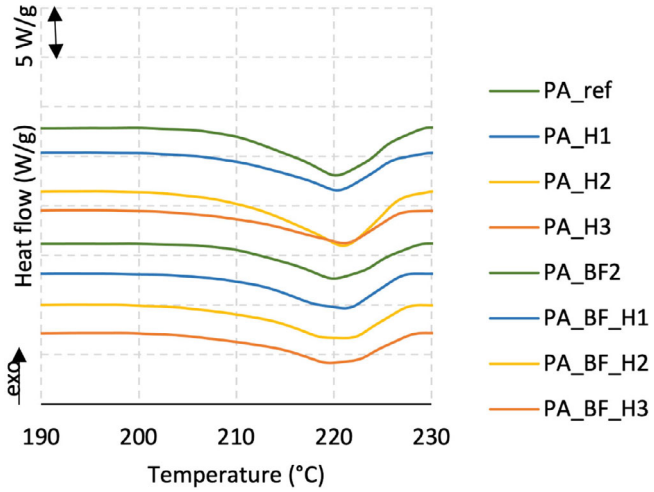

FIGURE 2 First heating curves of the samples.

does not change significantly. The explanation for this is that if the HNTs are distributed near the microfibers, the rigid amorphous interphase of the micro- and nanoscale reinforcement can overlap. With the increase of nanoparticle content, a further increment of the RAF is limited.

In the nanocomposites, the crystallization peak temperature and lamellar thickness slightly increase with increasing HNT content (Table 3). In hybrid composites, increasing nanoparticle content has a stronger effect on crystallization peak temperature and lamellar thickness. This suggests that halloysite nanoparticles are crystal nucleators. However, these changes in the peak temperature and lamellar thickness are so small that clear conclusions cannot be drawn.

There is only a slight difference in the crystal melting peak temperatures on the DSC curves of the samples (Figure 2), thus x-ray diffraction analysis was needed to obtain clear information about the crystal nucleating role of the reinforcing materials.

3.3 | X-ray diffraction

The diffractograms of the nanocomposites (Figure 3, a) show that the γ (020) crystals are missing, and in the samples reinforced with HNT, as halloysite content increases, peak α_2 ($2\theta = 23.6°$) flattens, and α_1 ($2\theta = 21.2°$) becomes dominant. This almost coincides with the highest intensity peak of the halloysite ($2\theta = 20.1°$),[12] and therefore promotes the growth of the α_1 peak. This confirms the crystal nucleating effect of the halloysite nanotubes since if the two peaks coincide, so does the distance of the crystal planes.

In the PA6 reinforced only with basalt fiber, the basalt fibers promote the increase of the γ (020) crystals at $2\theta = 23°$ (Figure 3B). Increasing the amount of halloysite nanotubes makes the α_1 peak more dominant, due to its crystal nucleating effect.

The above explains why the calculated size of the crystallites (Table 4) in the nanocomposites shows a minor increase with increasing halloysite content. There are outliers in the case of basalt fiber–reinforced composites, due to the function fitting method. However, the results obtained in the case of successfully fitted intensity peaks show an increase in the crystallite size of α_1-phase crystal modifications, while in the case of α_2, they decrease with increasing halloysite content.

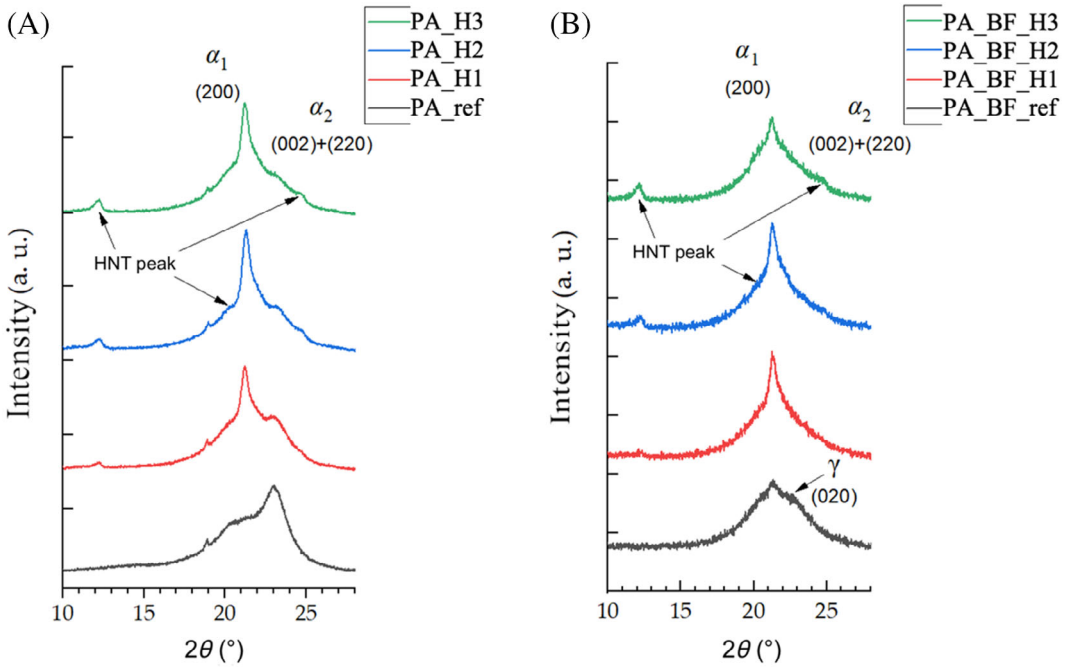

FIGURE 3 XRD diffractograms of (A) pure PA6 and nanocomposites and (B) basalt fiber reinforced and hybrid composites.

TABLE 4 Results of the XRD analysis: 2θ at the intensity peaks, half-width of the peaks (β), and the calculated size of the crystallites (L).

Sample	$2\theta_{(200)}$	$2\theta_{(002)+(220)}$	$\beta_{(200)}$	$\beta_{(002)+(220)}$	$L_{(200)}$	$L_{(002)+(220)}$
PA_REF	20.9	23.1	4.4	1.7	1.9	4.9
PA_H1	23.2	21.3	2.3	1.7	3.7	4.9
PA_H2	23.8	21.4	2.4	1.5	3.6	5.7
PA_H3	23.9	21.3	2.2	1.5	3.9	5.7
PA_BF	22.5	20.7	2.9	5.4	2.9	1.5
PA_BF_H1	24.4	21.4	1.7	1.8	5.1	4.6
PA_BF_H2	24.7	21.4	1.4	1.9	6.2	4.5
PA_BF_H3	23.3	21.2	4.5	3.2	1.9	2.7

3.4 | Scanning electron microscopy

The presence of aggregates in the nanocomposites is proven by the 1000x magnification SEM images of the fracture surfaces formed during the tensile test (Figure 4). Compared to the pure matrix, there was no significant change in the mode of failure; the fracture surfaces are segmented similarly. The aggregates are well embedded in the matrix, and the crack also went through the aggregates at the time of failure, which indicates that the aggregates are impregnated with the matrix material. The SEM images of the matrix reinforced with basalt fiber show that the matrix is less fragmented, and there are larger, flat surfaces, regardless of the nanoparticles. Also, some matrix material remained on some of the fibers after failure, which indicates an excellent adhesive bond between the fiber and the matrix. Moreover, there were no aggregates on the fracture surface, so the nanoparticles were probably uniformly distributed in the matrix. However, the presence of aggregates in the system cannot be ruled out, but they did not play a significant role in the fracture process.

Higher magnification shows a more detailed picture of the distribution of the nanoparticles (Figure 5). A magnification of 10,000 clearly shows that in composites containing only nanoparticles, the matrix has permeated the aggregates. In the hybrid composites, nano-sized formations appeared on the fracture surface, similar to those in the aggregate—they are nanoparticles. Overall, this means that the nanoparticles in the hybrid system show excellent dispersion.

3.5 | Transmission electron microscopy

We used transmission electron microscopy (TEM) to examine the samples reinforced with 1 wt% halloysite (HNT) (Figure 6D–F) and the unreinforced samples

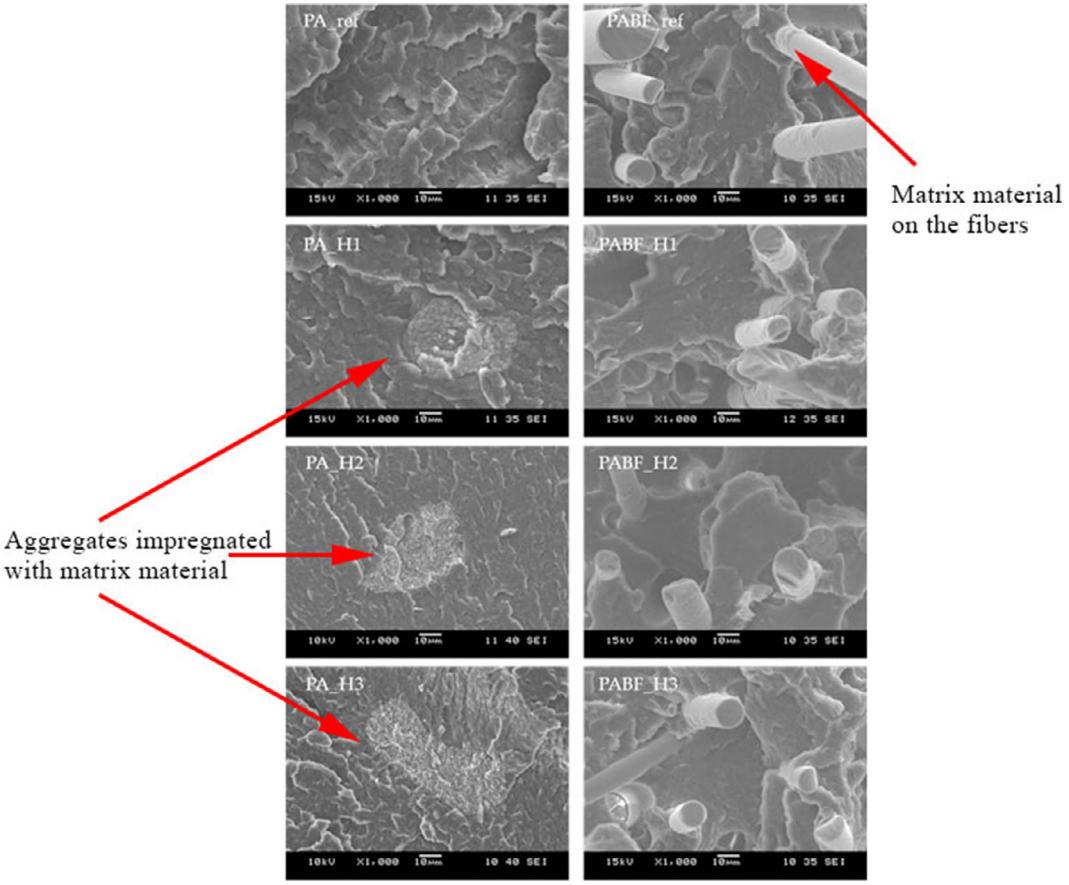

FIGURE 4 Typical surface area of nano- and hybrid composites with a PA 6 matrix after rupture at a magnification of 1000 (nominal).

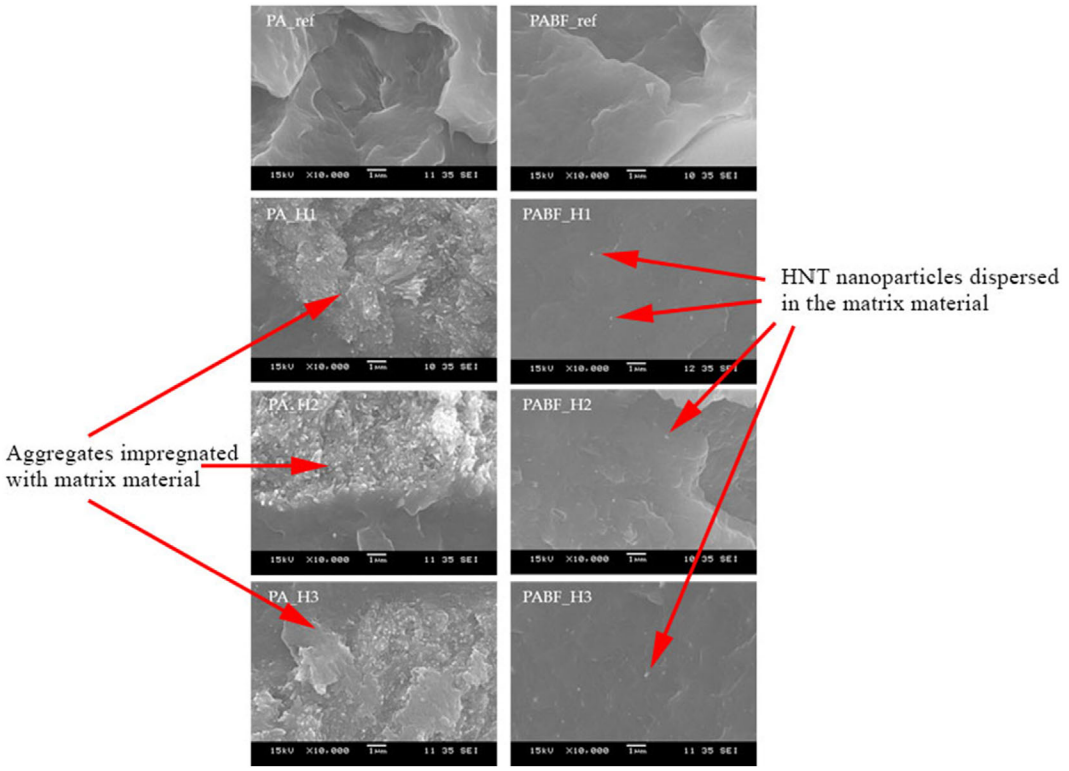

FIGURE 5 Typical surface area of nano- and hybrid composites with a PA 6 matrix after fracture at a magnification of 10,000 (nominal)

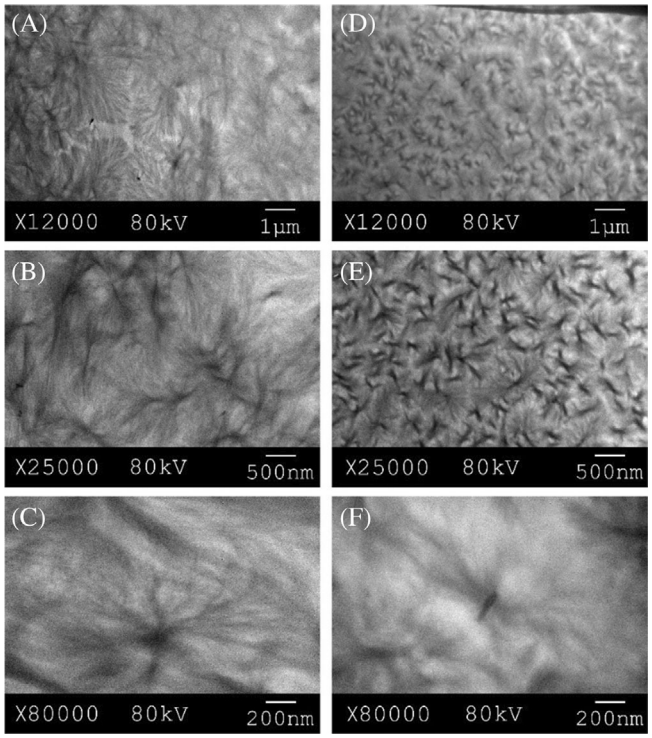

FIGURE 6 TEM images of (A–C) pure PA6 and (D–F) PA6 reinforced with 1 wt% HNT.

(Figure 6A–C) to see the spherulites caused by HNT in PA6.

Figure 6A–C shows the spherulite structure that formed during isothermal crystallization in the pure PA6. In the halloysite-reinforced composite sample, there are crystalline parts formed around individual nanoparticles (Figure 6D–F), which confirms the nucleating effect of the reinforcing material. Several smaller spherulites formed, each centered on a nanoparticle, and there are fewer and larger crystallites in the unreinforced PA6. Due to the sample preparation method for TEM, the images are not representative of the injection molded samples, so we cannot conclude the distribution of HNT or the probability of the appearance of aggregates that may have formed in the material. However, the crystal nucleating effect of HNTs is clear. Based on the DSC and TEM analyses, a microstructural model can be created (Figure 7), which shows that a rigid amorphous interphase is formed around the basalt fibers, while around the HNTs, a semi-crystalline and rigid amorphous interphase is created, and these interphases overlap with each other.

3.6 | Tensile properties of PA6/BF/HNT nano- and hybrid composites

The tensile behavior of the materials is better comparable by averaging the tensile curves point by point. In the

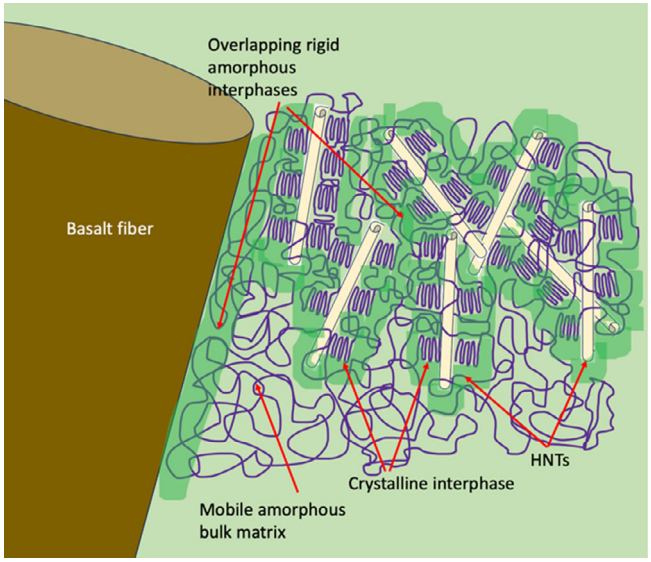

FIGURE 7 Schematic microstructure of PA6 reinforced by HNT.

composites containing only HNT nanoparticles, tensile strength and elongation at break decrease as HNT content increases. Still, there is a slight increase in the modulus. At the same time, in the composite containing basalt fibers as well, HNT nanoparticles also increased the modulus, and tensile strength, with a minimal decrease in elongation at break (Figure 8).

Table 5 contains the results of the tensile tests. The halloysite nanoparticles used alone slightly reduced elongation at break, but the standard deviation increased significantly. The reason can be traced back to the remaining aggregates, the size and number of which also show a random distribution. The average tensile strength decreased, while its standard deviation became larger, indicating the presence of aggregates because they act as a starting point of failure. On the other hand, the modulus slightly increased. Modulus is calculated for small deformations; the aggregates cannot play a significant role in load absorption due to their loose structure, and even reduce the load-bearing cross-section. This indicates that some of the nanoparticles are distributed in the matrix and can exert a strengthening effect, compensating for the weakening effect of the aggregates in the case of small deformations. The partial distribution and strengthening effect suggest a reasonable physical bond between the halloysite and PA 6.

The presence of the basalt fiber increased strength with a slight standard deviation. This indicates an excellent bond between the fiber and the matrix. The presence of halloysite nanoparticles next to the basalt fibers resulted in a small but clear increase in tensile strength, while the standard deviation was almost constant. The nanoparticles increased the tensile modulus of basalt

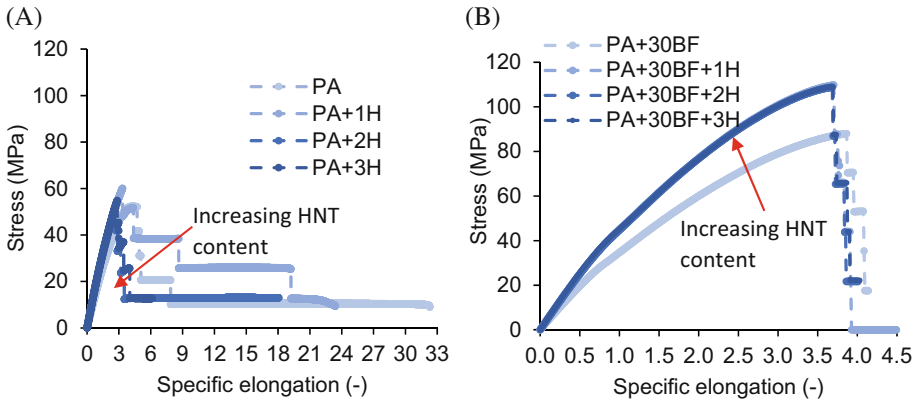

FIGURE 8 Averaged tensile curves of (A) the PA6 and the nanocomposites and (B) PA6 + 30BF and the hybrid composites.

TABLE 5 Tensile properties of the nano- and hybrid composites.

Sample	Tensile strength (MPa)	Tensile modulus (MPa)	Elongation at break (mm)
PA_ref	64.0 ± 0.5	2414 ± 70	5.1 ± 1.4
PAH1	64.9 ± 1.8	2457 ± 30	4.9 ± 2.5
PAH2	59.4 ± 5.4	2487 ± 25	2.8 ± 0.3
PAH3	61.0 ± 4.7	2513 ± 24	3.5 ± 1.2
PABF_ref	108.1 ± 0.9	5208 ± 103	3.7 ± 0.1
PABF_H1	112.3 ± 0.6	5541 ± 44	3.5 ± 0.1
PABF_H2	111.5 ± 0.9	5580 ± 91	3.5 ± 0.1
PABF_H3	112.2 ± 1.1	5766 ± 54	3.5 ± 0.1

fiber–reinforced samples by 300–500 MPa, which is comparable to the effect of traditionally used, artificially produced nanoparticles or additives.[27,28] Basalt fibers reduced elongation at break, but nanoparticles did not much decrease it further in hybrid composites. All this indicates a homogeneous distribution of the nanoparticles and an effective load transfer from the matrix to the fibers with the help of the HNTs and the overlapping interphases around the nano- and micro-sized reinforcing materials.

4 | CONCLUSIONS

In this study, we investigated the morphological and mechanical properties of hybrid composites with a PA6 matrix and reinforced with basalt fibers and halloysite nanotubes. The melt flow index (MFI) did not change significantly when only HNTs were added to the PA6 matrix. At the same time, in hybrid composites, higher HNT content resulted in a lower MFI. This indicates that in hybrid composites, the distribution of the nanoparticles was far more uniform, which was also reflected in the morphological characteristics of the materials.

In the hybrid composite, the ratio of the RAF was more significant compared to the nanocomposites. However, it did not increase with higher HNT content. This is because the rigid amorphous interphases near the micro- and nanosized reinforcement overlap with each other. X-ray diffraction analysis and transmission electron microscopy showed the crystal nucleating effect of the halloysite nanotubes. This indicates that around the basalt fibers, an RAF interphase formed, while around the nanoparticles, there was a two-layer interphase, the inner layer of which was semi-crystalline, while the outer layer was rigid amorphous. The nanoparticles are surrounded by a semi-crystalline interphase surrounded by a rigid amorphous interphase, which overlaps with the rigid amorphous interphase of the basalt fibers. Therefore, the halloysite nanotubes effectively help stress transfer from the matrix to the basalt fibers. The mechanical properties of the samples also reflected this; the hybrid composites had a significantly higher tensile modulus, tensile strength, and an unchanged elongation at break compared to the composite reinforced with only basalt fiber. With natural-based reinforcing materials it was possible to approach the increase in strength and modulus that is traditionally achieved with artificial materials.

ACKNOWLEDGMENTS

Project no. TKP-6-6/PALY-2021 has been implemented with the support provided by the Ministry of Culture and Innovation of Hungary from the National Research, Development, and Innovation Fund, financed under the

TKP2021-NVA funding scheme. László Mészáros is thankful for the János Bolyai Research Scholarship of the Hungarian Academy of Sciences. The research was supported by the ÚNKP-23-5-BME-434 New National Excellence Program of the Ministry for Culture and Innovation from the source of the National Research, Development, and Innovation Fund. The authors acknowledge funding from the European Union's Horizon 2020 research and innovation program under Marie Skłodowska-Curie grant agreement no—872152 (GREEN MAP).

DATA AVAILABILITY STATEMENT

Data sharing is not applicable to this article as no new data were created or analyzed in this study.

REFERENCES

1. Tanpichai S. Recent development of plant-derived nanocellulose in polymer nanocomposite foams and multifunctional applications: a mini-review. *Express Polym Lett*. 2022;16:52-74.
2. Gomez-Caturla J, Montanes N, Quiles-Carrillo L, et al. Development of biodegradable PLA composites and tangerine peel flour with improved toughness containing a natural-based terpenoid. *Express Polym Lett*. 2023;17:789-805.
3. Semperger OV, Török D, Suplicz A. Development and analysis of an in-Mold coating procedure for thermoplastic resin transfer molding to produce PA6 composites with a multifunctional surface. *Period Polytech Mech Eng*. 2022;66:350-360.
4. Groetsch T, Maghe M, Creighton C, Varley RJ. Environmental, property and cost impact analysis of carbon fibre at increasing rates of production. *J Clean Prod*. 2023;382:135292.
5. Zhang L, Liu W, Jiang H, et al. Upcycling of carbon fiber-reinforced polymer composites. *Compos Sci Technol*. 2023;231:109824.
6. Liu H, Yu Y, Liu Y, et al. A review on basalt fiber composites and their applications in clean energy sector and power grids. *Polymers (Basel)*. 2022;14:2376.
7. Miao Y-C, Xing D, Xi X-Y, Yue X, Bai Y-X, Ma P-C. Development of conducting basalt fibre with polymer-based nanocomposite sizing. *Mater Today Commun*. 2020;23:101170.
8. Singha K. A short review on basalt fiber. *Int J Text Sci*. 2012;1:19-28.
9. Jamshaid H, Mishra R. A green material from rock: basalt fiber – a review. *J Text Inst*. 2016;107:923-937.
10. Boro U, Moholkar VS. Antimicrobial bionanocomposites of poly(lactic acid)/ZnO deposited halloysite nanotubes for potential food packaging applications. *Mater Today Commun*. 2022;33:104787.
11. Tan D, Yuan P, Liu D, Du P. Chapter 8 – Surface modifications of Halloysite. In: Yuan P, Thill A, Bergaya F, Bergaya CS, eds. *Nanosized Tubular Clay Minerals – Halloysite and Imogolite*. Elsevier; 2016:167-201.
12. Fakhruddin K, Hassan R, Khan MUA, et al. Halloysite nanotubes and halloysite-based composites for biomedical applications. *Arab J Chem*. 2021;14:103294.
13. Liu M, Guo B, Du M, Jia D. Drying induced aggregation of halloysite nanotubes in polyvinyl alcohol/halloysite nanotubes solution and its effect on properties of composite film. *Appl Phys A Mater Sci Process*. 2007;88:391-395.
14. Lee J-W, Yu T, Park S-J, Kim Y-H. Interfacial properties of aramid/basalt fiber reinforced hybrid composites by addition of Halloysite nanotube. *Mod Phys Lett B*. 2019;33:1940031.
15. Franciszczak P, Taraghi I, Paszkiewicz S, Burzyński M, Meljon A, Piesowicz E. Effect of Halloysite nanotube on mechanical properties, thermal stability and morphology of polypropylene and polypropylene/short Kenaf fibers hybrid biocomposites. *Materials (Basel)*. 2020;13:4459.
16. Mallick PK, ed. Chapter 5 – Thermoplastics and thermoplastic–matrix composites for lightweight automotive structures. *Mallick Design and Manufacturing for Lightweight Vehicles*. Second ed. Woodhead Publishing; 2021:187-228.
17. Faghihi M, Shojaei A, Bagheri R. Characterization of polyamide 6/carbon nanotube composites prepared by melt mixing-effect of matrix molecular weight and structure. *Compos B: Eng*. 2015;78:50-64.
18. Kiziltas A, Liu W, Tamrakar S, Mielewski D. Graphene nanoplatelet reinforcement for thermal and mechanical properties enhancement of bio-based polyamide 6, 10 nanocomposites for automotive applications. *Compos Part C: Open Access*. 2021;6:100177.
19. Semperger OV, Suplicz A. The effect of the parameters of T-RTM on the properties of polyamide 6 prepared by in situ polymerization. *Materials (Basel)*. 2020;13:13010004.
20. Petrény R, Almásy L, Mészáros L. Investigation of the interphase structure in polyamide 6–matrix, multi-scale composites. *Compos Sci Technol*. 2022;225:109489.
21. Di Lorenzo ML, Righetti MC. Crystallization-induced formation of rigid amorphous fraction. *Polym Cryst*. 2018;1:e10023.
22. Benz J, Bonten C. Rigid amorphous fraction caused by particle–polymer–interaction in highly filled plastics. *AIP Conf Proc*. 2020;2289:20012.
23. Fornes T, Paul D. Crystallization behavior of nylon 6 nanocomposites. *Polymer (Guildf)*. 2003;44:3945-3961.
24. Itoh T, Miyaji H, Asai K. Thermal properties of α- and γ-forms of nylon 6. *Jpn J Appl Phys*. 1975;14:206-215.
25. Mandelkern L. *Crystallization of Polymers: Volume 2: Kinetics and Mechanisms, 2. Kiad*. Cambridge University Press; 2004.
26. Petrény R, Mészáros L. Moisture dependent tensile and creep behaviour of multi-wall carbon nanotube and carbon fibre reinforced, injection moulded polyamide 6 matrix multi-scale composites. *J Mater Res Technol*. 2022;16:689-699.
27. Zhou S, Wang J, Wang S, et al. Facile preparation of multiscale graphene-basalt fiber reinforcements and their enhanced mechanical and tribological properties for polyamide 6 composites. *Mater Chem Phys*. 2018;217:315-322.
28. Yu S, Oh KH, Hong SH. Effects of silanization and modification treatments on the stiffness and toughness of BF/SEBS/PA6,6 hybrid composites. *Compos B: Eng*. 2019;173:106922.

How to cite this article: Mészáros L, Bezerédi Á, Petrény R. Modifying the properties of polyamide 6 with high-performance environmentally friendly nano- and microsized reinforcing materials. *Polym Compos*. 2024;45(7):6404-6413. doi:10.1002/pc.28205